

Go with the Flows: Mixtures of Normalizing Flows for Point Cloud Generation and Reconstruction

Janis Postels*
ETH Zurich

jpostels@vision.ee.ethz.ch

Mengya Liu*
ETH Zurich

mengya.liu@vision.ee.ethz.ch

Riccardo Spezialetti
University of Bologna

riccardo.spezialetti@unibo.it

Luc Van Gool
ETH Zurich

vangool@vision.ee.ethz.ch

Federico Tombari
Google

tombari@google.com

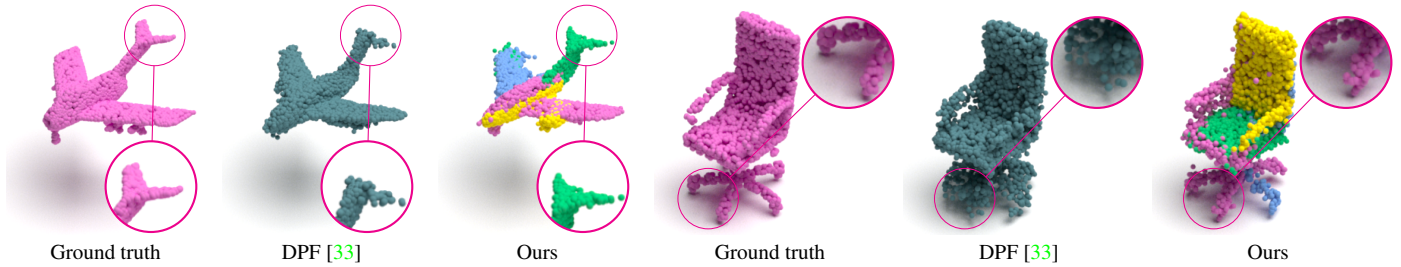


Figure 1. Our method (Ours) uses mixtures of Normalizing Flows (NFs) to accurately generate point clouds of a given object category, bringing advantages in preserving fine geometrical details compared to the use of a single flow (DPF [33]). Each mixture component learns to specialize in a distinct subregion in an unsupervised fashion.

Abstract

Recently Normalizing Flows (NFs) have demonstrated state-of-the-art performance on modeling 3D point clouds while allowing sampling with arbitrary resolution at inference time. However, these flow-based models still require long training time and large models for representing complicated geometries. This work enhances their representational power by applying mixtures of NFs to point clouds. We show that in this more general framework each component learns to specialize in a particular subregion of an object in a completely unsupervised fashion. By instantiating each mixture component with a comparatively small NF we generate point clouds with improved details compared to single-flow-based models while using fewer parameters and considerably reducing the inference runtime. We further demonstrate that by adding data augmentation, individual mixture components can learn to specialize in a semantically meaningful manner. We evaluate mixtures of NFs on generation, autoencoding and single-view reconstruction based on the ShapeNet dataset.

*equal contribution

1. Introduction

Over the last few years the field of image content generation has been revolutionized by learned generative models. Techniques such as Variational Autoencoder (VAE) [32], Generative Adversarial Network (GAN) [17] and Normalizing Flows (NFs) [12], have shown impressive results on a variety of applications [26, 54, 3]. In contrast, state-of-the-art proposals for 3D shape generation still have limitations in modeling the complex distribution of 3D shapes especially when 3D data is represented as point clouds [1]. This is mainly due to the lack of a regular underlying grid structure which inhibits the direct generalization of powerful convolution-based generative tools to 3D data. However, nowadays point clouds denote an increasingly popular data format for 3D shapes, as many modern 3D scanning devices, such as LiDARs and RGB-D cameras, output point clouds [21]. Thus, a generative model that can sample shapes represented as point clouds is valuable for several 3D computer vision down-stream tasks such as shape completion, synthesis and up-sampling.

To tackle this problem, prior work handled the irregular structure of point clouds by generating shapes with a fixed number of points by means of GANs or auto-regressive models [1, 15, 56, 43, 14]. Recently, another family of

generative models, NFs, has gained attention due to their appealing properties [54, 40, 33]. On the one hand, at inference time they naturally allow trading off runtime with resolution by adapting the number of generated points. On the other hand, their invertibility allows training them by directly minimizing the negative log-likelihood of the data, which leads to an improved training stability over GANs [1]. Typically, the point cloud distribution is modeled as a distribution of distributions [54, 33] in the framework of VAEs, where the decoder parameterizes an individual point cloud, *i.e.* distribution of points, conditioned on a sample from the (latent) distribution of shapes.

While the application of continuous [54] and discrete [33] NFs yielded state-of-the-art performance on shape generation and reconstruction benchmarks, they still come with the caveat of high computational costs, *e.g.* training [33] on ShapeNet [6] takes longer than a week. One root cause for this is related to the strength of NFs, *i.e.* their invertibility. Transforming a standard Gaussian using an invertible map into an arbitrarily complex geometry (*e.g.* including holes or multiple modes) with arbitrary precision requires squeezing or expanding space infinitely strong [13, 10]. To achieve this, one must resort to very deep NFs [10].

To accelerate the applicability of NFs to practical problems, this work proposes a novel decoder that generates a point cloud using a mixture of NFs. Similar to how our visual system decomposes shapes into parts [23, 25], in these mixtures multiple NFs learn to compose a final shape as the product experts. Each NF specializes in a shape sub-region in an unsupervised fashion, as illustrated in fig. 1, where the color indicates the NF from which a point originated. Moreover, our approach naturally inherits the ability of generating an arbitrary number of points, which clearly differentiates it from [19]. This also alleviates the problem of mismatching abstract geometric properties of the source distribution and the target distribution by learning to sew together the final object using several invertible maps. Furthermore, the resulting generative model exhibits interesting clustering properties that potentially enable broad applications such as unsupervised object part segmentation, semantic correspondence, 3D style transfer, etc.

We demonstrate that mixtures of NFs introduced in section 3 generalize and provide superior representational power compared to single-flow-based models at similar parameter count, while reducing the inference runtime. Furthermore, we show that this increased representational strength manifests itself in improved details on the generated/reconstructed point clouds resulting from individual NFs specializing in subregions of the 3D shapes.

2. Related Work

2.1. Mixtures of Normalizing Flows

Normalizing flows [42, 11, 12] are a class of generative models that allow efficient likelihood evaluation using invertible transformations. Recently, they have fueled a variety of applications [31, 8, 35, 53]. Despite their popularity, there have been surprisingly few works on mixtures of NFs [13, 10, 16, 27], all focused on toy data problems. As the first paper on mixtures of NFs, [13] separates the space into disjoint subsets using piece-wise linear activation functions to let each flow specialize on one subset. However, the discontinuity arising from partitioning leads to training difficulties [10]. In turn, [10] relaxes the invertibility constraint of NFs by introducing additional continuous latent variables and demonstrates improved performance on MNIST and CIFAR10. Further, [16] trains a mixture of NFs by following a boosting strategy, where each flow learns the current residual likelihood. Note that our work refrains from applying [10] or [16] since the continuous nature of the latent variables [10] and the iterative training procedure [16] do not allow obtaining well separated clusters. The mixture of NFs trained in [39] is closest to ours. However, they operate on toy data and the latent variables of their VAE only encompass the mixture weights whereas our VAE’s continuous latent variables encode 3D shapes on which we condition the mixture of NFs including its mixture weights. Lastly, [27] uses a Gaussian mixture model as the base distribution for a NF and applies this scheme to semi-supervised learning.

2.2. Generative Models for Point Clouds

Due to the unorganized structure of point clouds, pioneering generative models treat point clouds as a set of 3D points organized into a $N \times 3$ matrix, where N is fixed [1, 15, 56, 43, 14, 46, 49]. For example, Gadelha *et al.* [15] combine a multi-resolution encoder-decoder to form a VAE [32] for point cloud generation. Achlioptas *et al.* [1] explore the use of GANs [17, 20] to generate point clouds in the 3D euclidean space as well as in the latent space of a pre-trained auto-encoder. However, generating a point cloud with a fixed number of points limits the ability in producing complex shapes. This issue has been partially mitigated with the introduction of *plane-folding* decoders [19, 55], which learn to deform 2D points sampled from a grid into a set of 3D points. Thanks to this strategy, these methods can generate shapes with an arbitrary number of points. However, the above methods [4, 49, 46] rely on heuristic set distances such as the Chamfer distance (CD) and the Earth Mover’s distance (EMD), which both lead to several draw-backs [54, 5]. Indeed, while the CD favors point clouds that are concentrated in the mode of the marginal point distribution, the EMD is often computed by approximations and thus can

lead to biased gradients. As an alternative, a point cloud can be represented as a set of samples drawn from a point distribution. PointGrow [46] proposes an auto-regressive framework to operate recurrently with each point being sampled according to an estimated conditional distribution given all the preceding points. Moreover, ShapeGF [5] applies an energy-based framework to model a shape by learning the gradient field of its log-density and recover the distributions of the points. [45] models point clouds using conditional NFs. However, they do not learn the low-dimensional shape embeddings leading to poor performance compared to related work. PointFlow [54] employs continuous NFs [7, 18] to learn two distributions: the distribution of shapes and the distribution of points given a shape. [44] generates the weights of the continuous NF using a hypernetwork paired with a spherical log-normal base distribution achieving similar results as PointFlow. Similarly, Discrete Point Flow (DPF) [33] is also based on a VAE, but uses *discrete* affine coupling layers to avoid the computationally expensive solvers for differential equations, resulting in a significant speed-up of the method. Pumarola *et al.* [40] proposes a novel conditioning scheme for NFs to address 3D reconstruction and rendering from point clouds. Recently, SoftFlow [28] adds noise of varying magnitude to the input data and uses the noise magnitude as a condition. Our method shares the intuition of other flow-based methods, but overcomes limitations arising from using a single flow to model complex geometries by representing a shape as a mixture of NFs. Concurrently to this work, [29] proposes the use of multiple continuous NFs for point clouds which, similar to PointFlow, suffers from long training times. Note, that they do not train a mixture of NFs, but rather an unrelaxed version of it where each point is uniquely assigned to one flow. Finally, [37] also proposes multiple invertible maps for point clouds. However, they focus on reconstruction - without learning a generative model - and rely on a set of handcrafted optimization objectives instead of maximizing log-likelihood.

3. Mixtures of Normalizing Flows for Point Clouds

This section introduces mixtures of NFs for modeling point clouds. Initially, we revisit VAEs [32], which are used to approximate the distribution of point clouds, and NFs. Then, we discuss how we instantiate the individual components of a VAE - namely the encoder, decoder and prior.

3.1. Background

Normalizing Flows [42, 11, 12] are explicit generative models that learn to transform a simple base distribution $p(y)$ (e.g. standard Gaussian $\mathcal{N}(0, 1)$) into a complicated data distribution $p(x)$ (e.g. point cloud) using a series of n invertible transformations $f = f_{n-1} \circ \dots \circ f_0$ with $f : y \mapsto x$.

Hereby, the f_i are designed such that they allow efficient evaluation of the log-determinant of their Jacobian. Thus, using the change of variable formula we can train NFs by directly minimizing the negative log-likelihood of the data $-\log(p_f(x))$ under the model

$$\begin{aligned} \mathcal{L}(\theta) &= E_{x \sim p(x)} [-\log(p_f(x))] \\ &= -E_{x \sim p(x)} \left[\log(p(y)) - \sum_{i=0}^{n-1} \log \left(\det |J_{f_i^{-1}}(x)| \right) \right] \end{aligned} \quad (1)$$

where θ denotes the parameters of the invertible maps and $y = f^{-1}(x)$. A common choice for the invertible transformation is the so-called coupling layer [12]. Given an input $z \in \mathbb{R}^d$ a coupling layer c splits the dimensions of y into two sets $L \subset \{1, \dots, d\}$ and $K \subset \{1, \dots, d\}$ with $L \cup K = \emptyset$. It then applies the identity mapping to one set of dimensions $c(y^L) = y^L$. The other set of features is scaled by $s = s(y^L)$ and translated by $t = t(y^L)$ such that $c(y^K) = s(y^L) \odot y^K + t(y^L)$ where $s(y^L)$ and $t(y^L)$ are typically implemented using (non-invertible) multilayer perceptrons (MLPs). Calculating the log-determinant of the Jacobian of this transformation is then equivalent to summing its scaling factors $\log(\det |J_c(y)|) = \sum_{k \in K} s_k(y^L)$. Above model can further be extended to a conditional NF. Conditioning a NF on a variable z is commonly achieved [2] by introducing conditional scaling and translation in each coupling layer - $t(y; z)$ and $s(y; z)$ - and/or parameterizing the mean and the diagonal covariance matrix of the base distribution as functions of z , i.e. $p(y|z) = \mathcal{N}(y; \mu(z), \Sigma(z))$. Here, we follow [33] and apply both mechanisms.

Variational Autoencoders [32] are latent variable models that approximate a data distribution $p(x)$ by minimizing the negative Evidence Lower BOund (ELBO)

$$\begin{aligned} -ELBO(\theta, \psi, \phi) &= E_{z \sim p(z|x)} [-\log(p_\theta(x|z))] \\ &\quad + D_{KL}(p_\phi(z|x) || p_\psi(z)) \\ &= \mathcal{L}_D + \mathcal{L}_{Prior} \end{aligned} \quad (2)$$

Here, D_{KL} is the Kullback-Leibler divergence, $p_\phi(z|x)$ denotes an encoder parameterizing the approximate posterior distribution, $p_\psi(z)$ is a prior distribution of z and $p_\theta(x|z)$ is a decoder model parameterizing the distribution of x conditioned on z . While the prior distribution is often fixed (e.g. standard Gaussian $\mathcal{N}(0, 1)$), this work chooses the more flexible approach of learning its parameters.

3.2. Method

Our goal is to model a distribution $p(X)$ of 3D point clouds $X \in \mathbb{R}^{N \times 3}$ where each point cloud itself represents a distribution $p(x)$ over points $x \in \mathbb{R}^3$ in 3D space. We follow prior work [54, 33] applying NFs to point clouds

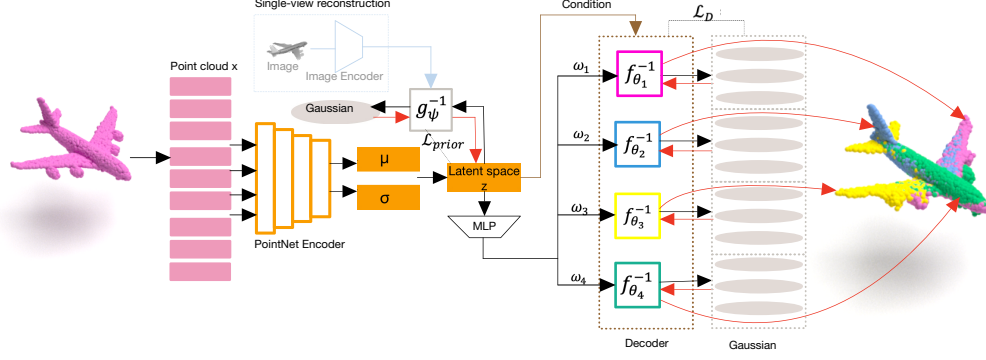


Figure 2. Model architecture. Black arrows indicate the training process, while red arrows represent the sampling of a point cloud from our model. During training, PointNet encodes a point cloud X to infer a posterior distribution $p_\phi(z|X)$ which can be seen as a distribution over shapes. A prior distribution parameterized by a NF g_ψ^{-1} is trained by maximizing the log-likelihood of z . When training single-view reconstruction (SVR), we condition g_ψ^{-1} on an image encoding. The decoder is parameterized as a mixture of NFs conditioned on z where each flow $f_{\theta_i}^{-1}$ learns to specialize in a subregion of the shape. Our model is optimized end-to-end by minimizing $\mathcal{L} = \mathcal{L}_{prior} + \mathcal{L}_D$.

and model $p(X)$ using a VAE. Subsequently, in this context $z \in \mathbb{R}^d$ refers to a d -dimensional latent representation of the entire point cloud. The overall architecture is depicted in fig. 2. Our main contribution is the decoder model which we implement as a mixture of conditional NFs that learn to specialize in distinct subregions of the point cloud in an unsupervised fashion. Subsequently, we discuss each component of the VAE in more details.

Decoder. Prior work learned the point cloud/distribution conditioned on the latent variable z using either a single continuous [55] or discrete [33] NF. While this yields strong performance, using a single (conditional) NF to transform a standard Gaussian $\mathcal{N}(0, 1)$ into complicated geometries, that potentially incorporate holes and/or multimodality, has fundamental limitations [13, 10]. Using invertible transformations to map a standard Gaussian into structures that incorporate multimodality or holes requires infinite bi-Lipschitz constants in the limit of arbitrary precision [10]. We refer to the supplement for a more detailed explanation and an intuitive example. To achieve such bi-Lipschitz constants, it is necessary to use large/deep NFs which limit their practical relevance. To bypass this shortcoming, one could either use a prior distribution with a more similar geometry to the target distribution or a mixture of NFs. The former requires dynamically adapting the prior distribution to the geometry of the target distribution, leading to a chicken-and-egg problem. Therefore, we choose to model the decoder as a mixture of NFs, learning to generate a point cloud $p(x)$ using several independent invertible maps. Formally, we model the conditional target distribu-

tion $p_\theta(x|z)$ in eq. (1) using a mixture of m conditional NFs

$$p(x|z) = \sum_{i=0}^m w_i(z) \mathcal{N}(f_{\theta_i}^{-1}(x); \mu(z), \Sigma(z)) \det |J_{f_{\theta_i}^{-1}}(x; z)| \quad (3)$$

where f_{θ_i} denotes the i -th NF with its parameters θ_i , $\mathcal{N}(f_{\theta_i}^{-1}(x); \mu(z), \Sigma(z))$ is the likelihood under the shared prior distribution and $w_i(z)$ are the mixture weights as a function of the latent variable z limited to $\sum_{i=0}^m w_i = 1$. Note that it is important to condition the mixture weights on the latent shape representation, since applying the same mixture weights across all shapes is very restrictive. Consequently, the first part of eq. (2) becomes

$$\mathcal{L}_D = E_{z \sim p_\phi} \left[\log \left(\sum_{i=0}^m w_i(z) \mathcal{N}(f_{\theta_i}^{-1}(x); \mu(z), \Sigma(z)) * \det |J_{f_{\theta_i}^{-1}}(x; z)| \right) \right] \quad (4)$$

Encoder. The encoder $p_\phi(z|X)$, also referred to as approximate posterior distribution, predicts a distribution over latent variables z given a point cloud X . We parameterize the posterior distribution with a normal distribution $\mathcal{N}(z; \mu(X), \Sigma(X))$. The mean $\mu(X)$ and the diagonal covariance matrix $\Sigma(X)$ are computed by a permutation invariant version of PointNet [41].

Prior. The prior distribution $p_\psi(z)$ - also referred to as shape prior in related work - specifies a distribution of latent representations of point clouds. Ideally, we want this distribution to match the marginal distribution of latent representations of real point clouds after the training in order to generate realistic point clouds at inference time. Therefore, we opt for a learned prior distribution [8] parameterized by a NF g_ψ with parameters ψ . When modeling distributions

of point clouds we use an unconditional NF. However, in our experiments on single-view reconstruction (SVR) we condition the prior distribution on a latent representation of the image/view and, thus, use a conditional NF. Combining this with our parameterization of the approximate posterior distribution yields the following prior loss:

$$\begin{aligned}\mathcal{L}_{Prior} &= -\mathcal{H}(p_\phi) - \mathbb{E}_{z \sim p_\phi(z|X)} [\log(p_\psi(z))] \\ &= -\frac{d}{2} \log(2\pi) - \frac{1}{2} \sum_{i=1}^d \log(\Sigma(X)) \\ &\quad - \mathbb{E}_{z \sim p_\phi} \left[\log(\mathcal{N}(g_\psi^{-1}(z))) \right. \\ &\quad \left. + \log(\det |J_{g_\psi^{-1}}(z)|) \right]\end{aligned}\quad (5)$$

4. Experiments

In this section, we evaluate the performance of our model on three tasks: point cloud generation section 4.1, autoencoding section 4.2, and SVR section 4.3. Further, we show that mixtures of NFs learn to specialize in a semantically meaningful and consistent manner section 4.4 and yield increasing benefit when decreasing the model size section 4.5.

Dataset. We conduct all the experiments using the normalized version of ShapeNet dataset [6] provided by [33]. For more details, please refer to the supplementary material.

Evaluation Metrics. Following the evaluation proposed by [1, 33, 54, 14], we measure the quality of reconstructed shapes, in section 4.2 and section 4.3, in terms of Chamfer Distance (CD) and Earth Mover’s Distance (EMD). However, these metrics were demonstrated to have severe limitations due to their sensitivity to outliers [48, 1]. For this reason, we include the more robust F1-score [34] that measures the percentage of points that are correctly reconstructed [48], *i.e.* the euclidean distance between each predicted point and the ground truth under a certain threshold τ . Following prior work [1, 54, 33], we evaluate generative modelling performance in section 4.1 by comparing generated and reference point clouds with the following metrics:

i) The *Jensen-Shannon divergence* (JSD) measures the similarity between two marginal point distributions obtained by taking the union of all generated (or reference) point clouds, and discretizing them to a voxel grid.

ii) *Coverage* (COV) measures the fraction of point clouds in the test set that are matched to at least one point cloud in the generated set. To establish the matching pairs, the nearest neighbor according to either CD or EMD is used.

iii) The *Minimum matching distance* (MMD) is the average distance of test point clouds to their nearest neighbor in the generated set according to the CD and EMD distances.

iv) *1-nearest neighbour accuracy* (1-NNA) is the leave-one-out accuracy of the 1-NN classifier in classifying the

generated and the reference point clouds as belonging to either of these two sets. As for the previous metrics, the nearest neighbor can be computed using either CD or EMD.

For more details we refer the reader to [1, 54]. While JSD and COV measure the diversity of the generated samples, MMD and 1-NNA aim at quantifying their perceptual quality. However, we observe that matches of MMD are typically highly dissimilar (see section 4.1). Consequently, MMD is unlikely to reflect the quality of high frequency components of generated point clouds. Therefore, we further evaluate generative modeling performance using the FID score [24] which quantifies both, perceptual quality and diversity. While there exists more advanced measures that disentangle perceptual quality and diversity [36], here we rely on the more well-known FID score which has been shown to correlate well with human perceptual scores on images. We compute the FID score on the features extracted by a DGCNN [52] pretrained on ShapeNet provided by [47].

Experimental setup. We use the same configuration of the encoder and prior as in DPF [33]. As in [33] we set the size D of the latent shape representation z to 128 for generation and 512 for both autoencoding and SVR. The decoder is a mixture of M NFs with each flow containing N conditioned affine coupling layers. These coupling layers compute scaling and translation, as discussed in section 3.1, using two fully connected layers with H hidden neurons, batch normalization and Swish activation functions. We modulate scaling and translation using an encoding of z according to FiLM [38, 33]. To ensure comparability with DPF [33] we enforce our method to have similar parameter count. Therefore, we reduce N and H in each of the M flows. In all experiments we follow [33] and set $N = 63$ and $H = 64$ for the single-flow model. A detailed description of the selection of H and N for mixtures of NFs can be found in the supplementary materials. We further refer to the supplement for an ablation study on the number M of mixture components. According to this study we found out that $M = 4$ performs well across all categories. Consequently, we use $M = 4$ in our experiments.

Baselines. On autoencoding and generation, we compare our method with existing models for point clouds including recent flow-based methods such as DPF [33] and PointFlow [54] as well as other popular works such as AtlasNet [19] and latent-GAN [1]. We retrained DPF [33] using the official implementation published by the authors due to the lack of pre-trained models. Results of other works are either obtained from [33] or using a pretrained model provided by the corresponding authors. On SVR, we compare our results against the most similar work in the literature, *i.e.* methods that reconstruct a shape from an image in form of a point cloud. This includes: AtlasNet [19], DCG [50], Pixel2Mesh [51] and DPF [33].

Oracle. Similar to DPF [33], we provide an "oracle" to quantify an upper bound on the performance of our model. In the evaluation of generative modeling the oracle compares a set point clouds obtained from the test set with one obtained from the training set. During the evaluation of autoencoding and SVR, the oracle provides a point cloud obtained by sampling from the ground truth.

Optimization. Details about the training can be found in the supplementary.

4.1. Generative Modeling

Experimental setup. We evaluate how well mixtures of NFs fit the distribution of point clouds. In line with prior work, we train a mixture of NFs on the three categories car, chair and airplane. We compute the evaluation metrics mentioned in section 4 between the test set and a set of generated point clouds of equal size. Each point cloud comprises 2048 points. We repeat the evaluation 10 times and report the average results. Results including standard deviation can be found in the supplementary.

Results. table 1 shows the results of this experiment. Mixtures of NFs obtain the best results regarding JSD, COV-CD/EMD and 1-NNA-EMD. Latent-GAN-CD/EMD [1] shows strong performance on MMD-CD/EMD while performing poorly on EMD/CD as expected since it is optimized using CD/EMD. Compared with other flow-based models, for which also evaluate the FID score, mixtures of NFs yield better performance than DPF [33] across most metrics and clearly outperform PointFlow [54]. fig. 3 shows qualitative examples when sampling from our model. Most importantly, we observe that each component of our mixture of NFs specializes in a distinct subregion of the shape. Interestingly, this specialization generalizes across different shapes.

Analysis of MMD. The role of the metrics MMD-CD/EMD is to quantify the perceptual quality of the generated point clouds. However, we question their reliability in this regard, since a qualitative examination reveals that matches between generated point clouds and test samples are dissimilar (see fig. 4). More, an ablation study in section 4.5 regarding the performance of models with fewer parameters reveals that the quality of the reconstructed point clouds clearly degrades with decreasing model size. However, in the supplement we further demonstrate that MMD-CD/EMD remain largely unchanged for smaller models despite an obvious degradation in the perceptual quality.

4.2. Autoencoding

Experimental setup. We evaluate mixtures of NFs on autoencoding. We train a mixture of NFs with 4 components on all categories of ShapeNet [6]. We report CD, EMD and F1-score ($\tau = 10^{-4}$) by following prior work in comparing test samples with 2048 points with their reconstructed

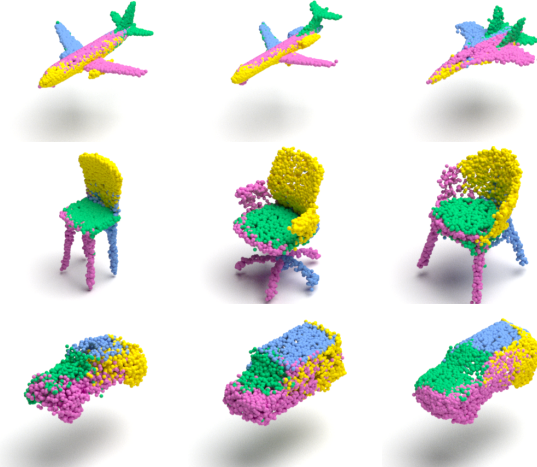


Figure 3. Qualitative results of generation. From above to below, we show samples generated with mixtures of NFs using models trained on the airplane, chair and car categories of ShapeNet [6].

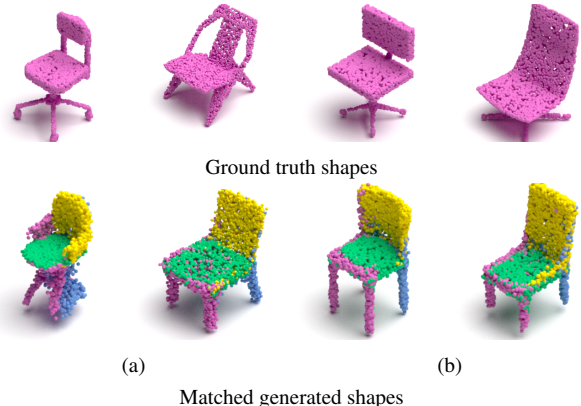


Figure 4. Failure cases of matches for ground truth shapes when computing MMD based on CD (a) and EMD (b). For each ground truth shape within the test set depicted (top row), searching for the most similar generated shape according to the CD and EMD distance yields clearly different matched shapes (bottom row). This supports the claim that MMD-CD/EMD do not clearly reflect the perceptual quality of generated point clouds.

version of equal size.

Results. In table 2 mixtures of NFs obtain the highest F1-score and second best CD/EMD. Moreover, we outperform latent-GAN [1] and PointFlow [54] across all metrics. AtlasNet [19] trained with CD as criteria performs the best on CD. As for EMD, we are slightly worse than DPF [33]. We argue that this is expected since EMD favors evenly distributed point clouds [33] which is simpler to achieve using a single NF. Conversely, we report a lower CD than DPF [33]. CD prioritizes regions [33], this reflects the ability of our model to better capture the local geometry of the shape, as qualitatively shown in fig. 1. By zooming into a specific part of the shape, we can see how our model precisely re-

Category	Method	JSD ↓	MMD ↓		COV ↑		1-NNA ↓		FID ↓
			CD	EMD	CD	EMD	CD	EMD	
Airplane	I-GAN-CD [1]	2.76	5.69	5.16	39.5	17.1	72.9	92.1	-
	I-GAN-EMD [1]	1.77	6.05	4.15	39.7	40.4	75.7	73.0	-
	PointFlow [54]	1.42	6.05	4.32	44.7	48.4	70.9	68.4	0.68
	DPF [33]	<u>1.14</u>	<u>6.03</u>	4.27	<u>46.4</u>	48.2	<u>70.3</u>	<u>67.5</u>	0.16
	Ours 4 Flows	1.03	6.06	<u>4.26</u>	46.5	48.4	70.1	66.9	0.15
	Oracle	0.50	5.97	3.98	51.4	52.7	49.8	48.2	0.074
Chair	I-GAN-CD [1]	3.65	16.66	7.91	42.3	17.1	68.5	96.5	-
	I-GAN-EMD [1]	1.27	<u>16.78</u>	5.75	44.3	43.8	66.6	<u>67.8</u>	-
	PointFlow [54]	1.51	17.15	6.20	43.3	46.5	67.0	70.4	0.29
	DPF [33]	<u>1.37</u>	17.24	6.13	<u>45.1</u>	46.0	64.8	68.2	0.26
	Ours 4 Flows	1.45	17.30	<u>6.11</u>	45.20	46.5	<u>65.3</u>	65.6	0.26
	Oracle	0.49	16.39	5.71	52.8	53.4	49.7	49.6	0.081
Car	I-GAN-CD [1]	2.65	8.83	5.36	41.3	15.9	62.6	92.7	-
	I-GAN-EMD [1]	1.31	<u>9.00</u>	4.40	38.3	32.9	<u>65.2</u>	63.2	-
	PointFlow [54]	0.59	9.53	4.71	42.3	35.8	70.1	74.2	0.20
	DPF [33]	<u>0.57</u>	9.67	<u>4.60</u>	40.8	<u>43.7</u>	71.29	66.0	0.11
	Ours 4 Flows	0.55	9.50	4.62	41.4	43.8	69.0	<u>64.8</u>	0.10
	Oracle	0.37	9.24	4.56	52.8	52.7	50.9	50.5	0.054

Table 1. Generative modeling. Comparison with related work. JSD and MMD-EMD are multiplied by 10^2 , MMD-CD is multiplied by 10^4

constructs fine-grained geometric details, conversely DPF [33] tends to get a smoother and noisier shape, this confirming our expectations as explained in the methodology section. For example, looking at the tail of the airplane and the legs of the chair, we can see how our method is able to reconstruct them completely and clearly, while DPF [33] fails at reconstructing high-frequency regions.

Method	CD ↓	EMD ↓	F1 ↑, $\tau = 10^{-4}$
I-GAN-CD [1]	7.07	7.70	-
I-GAN-EMD [1]	9.18	5.30	-
AtlasNet [19]	5.66	5.81	-
PointFlow [54]	7.54	5.18	32.3
DPF [33]	6.92	4.66	<u>34.5</u>
Ours 4 Flows	<u>6.88</u>	<u>4.80</u>	34.8
Oracle	3.10	3.13	76.0

Table 2. Autoencoding. Comparison with related work on the full ShapeNet dataset [6]. CD is multiplied by 10^4 , EMD by 10^2 .

4.3. Single-view Reconstruction

Experimental setup. We evaluate the ability of mixtures of NFs to reconstruct point clouds from a single RGB image. At test time we sample from the prior conditioned on the encoding of RGB test images and subsequently sample from the decoder conditioned on this sample. We re-

port CD, EMD and F1-score. Unlike in our experiments on autoencoding section 4.2, here we choose a threshold $\tau = 10^{-3}$ to ensure comparability with prior work.

Results. Quantitative results can be found in table 3. Generally, we observe that mixtures of NFs yield at least second best performance across all metrics. AtlasNet [19] outperforms our method for CD, which is expected since it explicitly optimizes this metric. Interestingly, mixtures of NFs demonstrate the best performance in F1-score, which is regarded as a more faithful metric for perceptual quality [34]. In fig. 5 we show qualitative examples of SVR using DPF [33] and mixtures of NFs. We observe that mixtures of NFs yield sharper reconstructions with particular improvements on complicated geometries, *e.g.* the lamp. Also for SVR we observe that in mixtures of NFs each flow learns to be responsible for one part of the shape.

Method	CD ↓	EMD ↓	F1 ↑, $\tau = 10^{-3}$
AtlasNet [19]	5.34	12.54	<u>52.2</u>
DCG [50]	6.35	18.94	45.7
Pixel2Mesh [51]	5.91	13.80	-
DPF [33]	5.80	11.17	52.0
Ours 4 Flows	<u>5.66</u>	<u>11.18</u>	52.3
Oracle	1.10	5.70	84.0

Table 3. Single-view Reconstruction. Comparison with related work on 13 categories of ShapeNet [6]. CD is multiplied by 10^3 , EMD is multiplied by 10^2 .

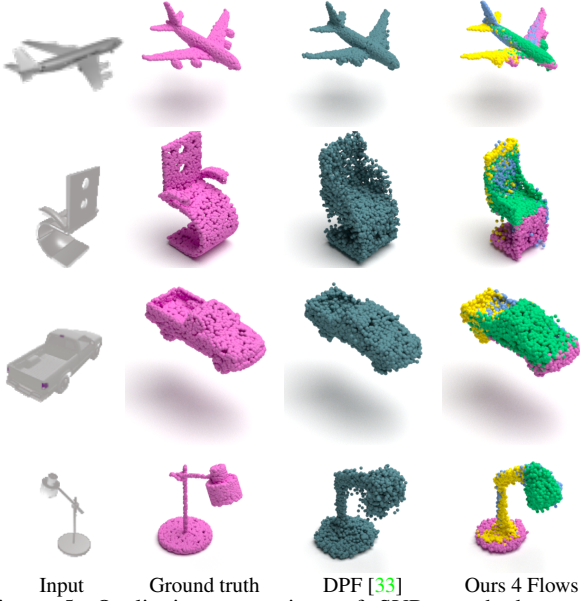


Figure 5. Qualitative comparison of SVRs methods on the ShapeNet [6] test set. On the left, we show the RGB view used as input. We also report the results for DPF [33].

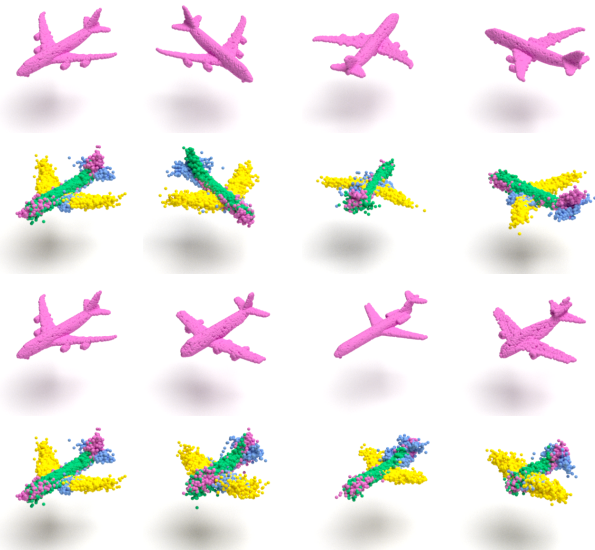


Figure 6. Qualitative examples of reconstructions on the ShapeNet [6] test set when training the autoencoding model with random rotations. The first two rows show the reconstructions obtained when applying random rotations to the same input point cloud. The third and fourth row show different test shapes and their reconstructions.

4.4. Rotation Invariant Latent Variables

This section qualitatively evaluates whether our mixtures of NFs can learn to specialize to semantically meaningful regions of the object, which is an interesting property that could aid applications such as point cloud registration.

Experimental setup. We train a mixture of 4 NFs following the setup used in the autoencoding experiments, using

the airplane category of ShapeNet [6]. Additionally, we augment the training data with random 3D rotations. After training, we qualitatively examine whether the mixture assignments are rotation invariant. If mixtures of NFs are able to specialize in a semantically meaningful way, we expect approximate rotational invariance.

Results. In fig. 6 we illustrate qualitative results for this experiment. Once the model is trained, we randomly rotate the input shapes before passing them through the model. We observe that different components of the mixture model learn to specialize in reconstructing different semantic parts of the airplanes (*e.g.* yellow \rightarrow wings, green \rightarrow center of the airplane). However, learning the distribution of randomly rotated 3D point clouds is a much harder task and this is reflected in slightly less detailed models reconstructed by our method, as can be seen in fig. 6.

4.5. Decreasing Number of Parameters

Based on prior work on NFs [13, 10] and our reasoning in section 3.2, mixtures of NFs yield increasing benefits in the regime of smaller decoder sizes. This experiment aims at verifying this intuition by comparing the reconstruction performance of DPF [33] with mixtures of NFs for decoders with decreasing number of parameters. We are particularly interested in the reconstruction performance since it directly measures the representational strength of the underlying model. We refer to the supplement for generation metrics associated with this experiment.

Experimental setup. We train DPF and mixtures of NFs using our generative modeling setup on the airplane category (see section 4) varying the size of the decoder. For DPF we use a decoder NF with 63 (original size), 24, 12 and 6 coupling layers and unchanged $H = 64$. We compare the reconstruction performance regarding the F1-score against a mixture of four NFs. H and N of the mixture are chosen such that it contains slightly fewer parameters. The detailed choice of H and N can be found in the supplement.

Results. In fig. 7 (a) we observe that the relative improvement in terms of reconstruction performance increases for smaller decoder. While the mixture of four NFs achieves a relative improvement over DPF [33] of 3.11% in the original size, decreasing the number of coupling layers to 6 more than doubles the relative improvement up to 7.65%.

4.6. Inference Runtime Comparison

Finally, we compare the inference runtime of mixtures of NFs against DPF [33] when using decoder models of comparable parameter size. Specifically, we measure the average time per generated point during sampling. fig. 7 (b) shows the relative inference runtime improvement depending on the size of the mixture. Since sampling of each point requires only a smaller NF the average runtime decreases with an increasing number of mixture components.

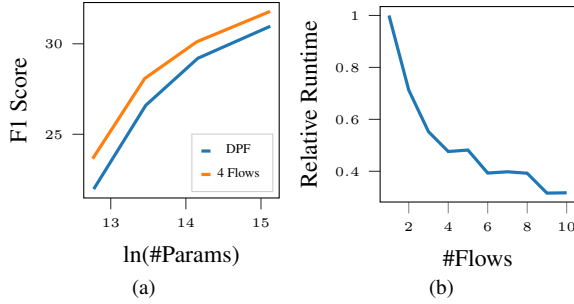


Figure 7. (a) Average reconstruction performance (F1-score) on the chair category of ShapeNet for DPF (blue) and a mixture of 4 NFs (orange) vs. the parameter count. The relative improvement increases for small decoder. (b) Relative inference runtime of mixtures of NFs compared with DPF at similar parameter count vs. the mixture size (#Flows). More components reduce the inference runtime since each point is sampled from a smaller network.

However, since the runtime of a NF mainly depends on the number of coupling layers, we do not observe an anti-proportional behaviour.

5. Conclusion

We proposed mixtures of NFs for modeling 3D point clouds. We showed that mixtures of NFs outperform models based on a single NF [54, 33] on generation, autoencoding and SVR (see section 4.2 & section 4.3). This resonates with theoretical insight that single-flow-based models struggle on complicated geometries [13, 10]. We showed that mixtures of NFs can bypass these shortcomings by learning to compose a shape as a product of experts. Moreover, we demonstrated that the relative improvements obtained by mixtures of NFs over single-flow-based models increase for smaller models.

Furthermore, we observe that mixtures of NFs exhibit other interesting properties. The specialization of mixture components generalizes across different shapes (e.g. the same flow is always responsible for the wings in fig. 6) and can be made rotational invariant by adding random rotations at training time. This implies that mixtures of NFs gain a deeper understanding of the underlying shape. This property potentially gives rise to interesting applications in point cloud registration - even between different objects of the same class as a semantically meaningful clustering approach - and is a promising direction for future research.

References

- [1] Panos Achlioptas, Olga Diamanti, Ioannis Mitliagkas, and Leonidas Guibas. Learning representations and generative models for 3d point clouds. In *International conference on machine learning*, pages 40–49. PMLR, 2018. 1, 2, 5, 6, 7, 14
- [2] Lynton Ardizzone, Carsten Lüth, Jakob Kruse, Carsten Rother, and Ullrich Köthe. Guided image generation with conditional invertible neural networks. *arXiv preprint arXiv:1907.02392*, 2019. 3
- [3] Diego Martin Arroyo, Janis Postels, and Federico Tombari. Variational transformer networks for layout generation. *Proceedings of the IEEE/CVF Conference on Computer Vision and Pattern Recognition*, 2021. 1
- [4] Heli Ben-Hamu, Haggai Maron, Itay Kezurer, Gal Avineri, and Yaron Lipman. Multi-chart generative surface modeling. *ACM Transactions on Graphics (TOG)*, 37(6):1–15, 2018. 2
- [5] Ruojin Cai, Guandao Yang, Hadar Averbuch-Elor, Zekun Hao, Serge Belongie, Noah Snavely, and Bharath Hariharan. Learning gradient fields for shape generation. *arXiv preprint arXiv:2008.06520*, 2020. 2, 3
- [6] Angel X Chang, Thomas Funkhouser, Leonidas Guibas, Pat Hanrahan, Qixing Huang, Zimo Li, Silvio Savarese, Manolis Savva, Shuran Song, Hao Su, et al. Shapenet: An information-rich 3d model repository. *arXiv preprint arXiv:1512.03012*, 2015. 2, 5, 6, 7, 8, 13
- [7] Ricky T. Q. Chen, Yulia Rubanova, Jesse Bettencourt, and David K Duvenaud. Neural ordinary differential equations. In *Advances in Neural Information Processing Systems*, volume 31, 2018. 3
- [8] Xi Chen, Diederik P Kingma, Tim Salimans, Yan Duan, Pratul Dhariwal, John Schulman, Ilya Sutskever, and Pieter Abbeel. Variational lossy autoencoder. *International Conference on Learning Representations*, 2017. 2, 4
- [9] Christopher B Choy, Danfei Xu, JunYoung Gwak, Kevin Chen, and Silvio Savarese. 3d-r2n2: A unified approach for single and multi-view 3d object reconstruction. In *European conference on computer vision*, pages 628–644. Springer, 2016. 13
- [10] Rob Cornish, Anthony Caterini, George Deligiannidis, and Arnaud Doucet. Relaxing bijectivity constraints with continuously indexed normalising flows. In *International Conference on Machine Learning*, pages 2133–2143. PMLR, 2020. 2, 4, 8, 9
- [11] Laurent Dinh, David Krueger, and Yoshua Bengio. Nice: Non-linear independent components estimation. *arXiv preprint arXiv:1410.8516*, 2014, 2014. 2, 3
- [12] Laurent Dinh, Jascha Sohl-Dickstein, and Samy Bengio. Density estimation using real nvp. *International Conference on Learning Representations*, 2017. 1, 2, 3
- [13] Laurent Dinh, Jascha Sohl-Dickstein, Razvan Pascanu, and Hugo Larochelle. A rad approach to deep mixture models. *arXiv preprint arXiv:1903.07714*, 2019. 2, 4, 8, 9
- [14] Haoqiang Fan, Hao Su, and Leonidas J Guibas. A point set generation network for 3d object reconstruction from a single image. In *Proceedings of the IEEE conference on computer vision and pattern recognition*, pages 605–613, 2017. 1, 2, 5
- [15] Matheus Gadelha, Rui Wang, and Subhransu Maji. Multiresolution tree networks for 3d point cloud processing. In *Proceedings of the European Conference on Computer Vision (ECCV)*, pages 103–118, 2018. 1, 2
- [16] Robert Giaquinto and Arindam Banerjee. Gradient boosted normalizing flows. *Advances in Neural Information Processing Systems*, 33, 2020. 2

- [17] Ian J Goodfellow, Jean Pouget-Abadie, Mehdi Mirza, Bing Xu, David Warde-Farley, Sherjil Ozair, Aaron Courville, and Yoshua Bengio. Generative adversarial networks. *arXiv preprint arXiv:1406.2661*, 2014. 1, 2
- [18] Will Grathwohl, Ricky TQ Chen, Jesse Bettencourt, Ilya Sutskever, and David Duvenaud. Ffjord: Free-form continuous dynamics for scalable reversible generative models. *International Conference on Learning Representations*, 2019. 3
- [19] Thibault Groueix, Matthew Fisher, Vladimir G Kim, Bryan C Russell, and Mathieu Aubry. A papier-mâché approach to learning 3d surface generation. In *Proceedings of the IEEE conference on computer vision and pattern recognition*, pages 216–224, 2018. 2, 5, 6, 7
- [20] Ishaan Gulrajani, Faruk Ahmed, Martin Arjovsky, Vincent Dumoulin, and Aaron Courville. Improved training of wasserstein gans. In *Proceedings of the 31st International Conference on Neural Information Processing Systems*, pages 5769–5779, 2017. 2
- [21] Yulan Guo, Hanyun Wang, Qingyong Hu, Hao Liu, Li Liu, and Mohammed Bennis. Deep learning for 3d point clouds: A survey. *IEEE transactions on pattern analysis and machine intelligence*, 2020. 1
- [22] Kaiming He, Xiangyu Zhang, Shaoqing Ren, and Jian Sun. Deep residual learning for image recognition. In *Proceedings of the IEEE conference on computer vision and pattern recognition*, pages 770–778, 2016. 12
- [23] Donald Olding Hebb. *The organization of behavior: A neuropsychological theory*. Psychology Press, 2005. 2
- [24] Martin Heusel, Hubert Ramsauer, Thomas Unterthiner, Bernhard Nessler, and Sepp Hochreiter. Gans trained by a two time-scale update rule converge to a local nash equilibrium. In *Proceedings of the 31st International Conference on Neural Information Processing Systems*, pages 6629–6640, 2017. 5
- [25] Donald D Hoffman and Whitman A Richards. Parts of recognition. *Cognition*, 18(1-3):65–96, 1984. 2
- [26] Phillip Isola, Jun-Yan Zhu, Tinghui Zhou, and Alexei A Efros. Image-to-image translation with conditional adversarial networks. In *Proceedings of the IEEE conference on computer vision and pattern recognition*, pages 1125–1134, 2017. 1
- [27] Pavel Izmailov, Polina Kirichenko, Marc Finzi, and Andrew Gordon Wilson. Semi-supervised learning with normalizing flows. In *International Conference on Machine Learning*, pages 4615–4630. PMLR, 2020. 2
- [28] Hyeonju Kim, Hyeonseung Lee, Woo Hyun Kang, Joun Yeop Lee, and Nam Soo Kim. Softflow: Probabilistic framework for normalizing flow on manifolds. *International Conference on Neural Information Processing Systems*, 2020. 3
- [29] Takumi Kimura, Takashi Matsubara, and Kuniaki Uehara. Chartpointflow for topology-aware 3d point cloud generation. *arXiv preprint arXiv:2012.02346*, 2020. 3
- [30] Diederik P Kingma and Jimmy Lei Ba. Adam: A method for stochastic gradient descent. In *ICLR: International Conference on Learning Representations*, pages 1–15, 2015. 13
- [31] Durk P Kingma, Tim Salimans, Rafal Jozefowicz, Xi Chen, Ilya Sutskever, and Max Welling. Improved variational inference with inverse autoregressive flow. *Advances in Neural Information Processing Systems*, 29:4743–4751, 2016. 2
- [32] Diederik P Kingma and Max Welling. Auto-encoding variational bayes. *arXiv preprint arXiv:1312.6114*, 2013. 1, 2, 3
- [33] Roman Klokov, Edmond Boyer, and Jakob Verbeek. Discrete point flow networks for efficient point cloud generation. In *16th European Conference on Computer Vision*, 2020. 1, 2, 3, 4, 5, 6, 7, 8, 9, 12, 13, 14, 15, 19, 21, 22
- [34] Arno Knapitsch, Jaesik Park, Qian-Yi Zhou, and Vladlen Koltun. Tanks and temples: Benchmarking large-scale scene reconstruction. *ACM Transactions on Graphics (ToG)*, 36(4):1–13, 2017. 5, 7
- [35] Andreas Lugmayr, Martin Danelljan, Luc Van Gool, and Radu Timofte. Srflo: Learning the super-resolution space with normalizing flow. In *European Conference on Computer Vision*, pages 715–732. Springer, 2020. 2
- [36] Muhammad Ferjad Naeem, Seong Joon Oh, Youngjung Uh, Yunje Choi, and Jaejun Yoo. Reliable fidelity and diversity metrics for generative models. In *International Conference on Machine Learning*, pages 7176–7185. PMLR, 2020. 5
- [37] Despoina Paschalidou, Angelos Katharopoulos, Andreas Geiger, and Sanja Fidler. Neural parts: Learning expressive 3d shape abstractions with invertible neural networks. *Proceedings of the IEEE/CVF International Conference on Computer Vision*, 2021. 3
- [38] Ethan Perez, Florian Strub, Harm De Vries, Vincent Dumoulin, and Aaron Courville. Film: Visual reasoning with a general conditioning layer. In *Proceedings of the AAAI Conference on Artificial Intelligence*, volume 32, 2018. 5, 12
- [39] Guilherme GP Pires and Mário AT Figueiredo. Variational mixture of normalizing flows. *arXiv preprint arXiv:2009.00585*, 2020. 2
- [40] Albert Pumarola, Stefan Popov, Francesc Moreno-Noguer, and Vittorio Ferrari. C-flow: Conditional generative flow models for images and 3d point clouds. In *Proceedings of the IEEE/CVF Conference on Computer Vision and Pattern Recognition*, pages 7949–7958, 2020. 2, 3
- [41] Charles R Qi, Hao Su, Kaichun Mo, and Leonidas J Guibas. Pointnet: Deep learning on point sets for 3d classification and segmentation. In *Proceedings of the IEEE conference on computer vision and pattern recognition*, pages 652–660, 2017. 4, 12
- [42] Danilo Rezende and Shakir Mohamed. Variational inference with normalizing flows. In *International Conference on Machine Learning*, pages 1530–1538. PMLR, 2015. 2, 3
- [43] Dong Wook Shu, Sung Woo Park, and Junseok Kwon. 3d point cloud generative adversarial network based on tree structured graph convolutions. In *Proceedings of the IEEE/CVF International Conference on Computer Vision*, pages 3859–3868, 2019. 1, 2
- [44] Przemysław Spurek, Maciej Zięba, Jacek Tabor, and Tomasz Trzciński. Hyperflow: Representing 3d objects as surfaces. *arXiv preprint arXiv:2006.08710*, 2020. 3

- [45] Michał Stypułkowski, Maciej Zamorski, Maciej Zięba, and Jan Chorowski. Conditional invertible flow for point cloud generation. *arXiv preprint arXiv:1910.07344*, 2019. 3
- [46] Yongbin Sun, Yue Wang, Ziwei Liu, Joshua Siegel, and Sanjay Sarma. Pointgrow: Autoregressively learned point cloud generation with self-attention. In *Proceedings of the IEEE/CVF Winter Conference on Applications of Computer Vision*, pages 61–70, 2020. 2, 3
- [47] An Tao. Unsupervised point cloud reconstruction for classific feature learning. <https://github.com/AnTao97/UnsupervisedPointCloudReconstruction>, 2020. 5
- [48] Maxim Tatarchenko, Stephan R Richter, René Ranftl, Zhuwen Li, Vladlen Koltun, and Thomas Brox. What do single-view 3d reconstruction networks learn? In *Proceedings of the IEEE/CVF Conference on Computer Vision and Pattern Recognition*, pages 3405–3414, 2019. 5
- [49] Diego Valsesia, Giulia Fracastoro, and Enrico Magli. Learning localized generative models for 3d point clouds via graph convolution. In *International conference on learning representations*, 2018. 2
- [50] Kaiqi Wang, Ke Chen, and Kui Jia. Deep cascade generation on point sets. In *IJCAI*, volume 2, page 4, 2019. 5, 7
- [51] Nanyang Wang, Yinda Zhang, Zhuwen Li, Yanwei Fu, Wei Liu, and Yu-Gang Jiang. Pixel2mesh: Generating 3d mesh models from single rgb images. In *Proceedings of the European Conference on Computer Vision (ECCV)*, pages 52–67, 2018. 5, 7
- [52] Yue Wang, Yongbin Sun, Ziwei Liu, Sanjay E. Sarma, Michael M. Bronstein, and Justin M. Solomon. Dynamic graph cnn for learning on point clouds. *ACM Transactions on Graphics (TOG)*, 2019. 5
- [53] Valentin Wolf, Andreas Lugmayr, Martin Danelljan, Luc Van Gool, and Radu Timofte. Deflow: Learning complex image degradations from unpaired data with conditional flows. *arXiv preprint arXiv:2101.05796*, 2021. 2
- [54] Guandao Yang, Xun Huang, Zekun Hao, Ming-Yu Liu, Serge Belongie, and Bharath Hariharan. Pointflow: 3d point cloud generation with continuous normalizing flows. In *Proceedings of the IEEE/CVF International Conference on Computer Vision*, pages 4541–4550, 2019. 1, 2, 3, 5, 6, 7, 9, 13, 14
- [55] Yaoqing Yang, Chen Feng, Yiru Shen, and Dong Tian. Foldingnet: Point cloud auto-encoder via deep grid deformation. In *Proceedings of the IEEE Conference on Computer Vision and Pattern Recognition*, pages 206–215, 2018. 2, 4
- [56] Maciej Zamorski, Maciej Zięba, Piotr Klukowski, Rafał Nowak, Karol Kurach, Wojciech Stokowiec, and Tomasz Trzcinski. Adversarial autoencoders for compact representations of 3d point clouds. *Computer Vision and Image Understanding*, 193:102921, 2020. 1, 2

Supplementary Material of "Go with the Flows: Mixtures of Normalizing Flows for Point Cloud Generation and Reconstruction"

Subsequently, we present further experimental results and details regarding mixtures of NFs for point clouds. Therefore, section 5 investigates the impact of varying the number of components in a mixture of NFs. In section 5 we give a detailed description of the training, optimization and architecture used in our experiments. Further, section 5 demonstrate additional results on generative modeling. In section 5 we show qualitative results of interpolating between latent representations of shapes, followed by the exploration of dense sampling with sparse input (see in section 5. section 5 presents an analytic toy example regarding the benefits of applying a mixture of NFs to point clouds as opposed to single-flow-based models. Lastly, we show more qualitative examples regarding generation, autoencoding and SVR in section 5, section 5 and section 5 respectively.

Ablation Study

We perform an ablation study regarding the number components n in a mixture of NFs. Therefore, we train mixtures of NFs using a varying number components n on the categories airplane ($n \in [1, 2, 4, 6, 8, 10]$), chair ($n \in [1, 4, 8]$), car ($n \in [1, 4, 8]$) and report reconstruction performance in terms of the F1-score (see table 4). We observe that any number > 1 leads to a clear improvement over a single-flow-based model. In our main experiments we choose $n = 4$ as it performs well across all categories. However, we also note that there appears to be no strong preference regarding the number of components. We interpret this as evidence that geometries on ShapeNet are not complex enough to benefit from a very large n .

Method	#flows	CD \downarrow	EMD \downarrow	F1 $\uparrow, \tau = 10^{-4}$
Airplane	1	2.90	3.53	60.68
	2	2.89	3.52	61.23
	4	2.88	3.50	61.07
	6	2.89	3.51	61.14
	8	3.05	3.49	61.24
	10	2.90	3.50	61.08
Chair	1	6.66	4.61	30.97
	4	6.45	4.53	31.94
	8	6.60	4.54	31.77
Car	1	7.41	4.44	21.20
	4	7.73	4.38	22.34
	8	7.75	4.39	21.22

Table 4. Auto-encoding. Ablation study on different number of NFs. CD is multiplied by 10^4 , EMD is multiplied by 10^2 .

Training Details

Architecture. We follow [33] and implement the *encoder* in all our experiments as a PointNet [41]. Our PointNet encoder consists of 5 layers with feature sizes of the layers set to 3, 64, 128, 256, 512. Subsequently, we perform max-pooling along the dimension of the points. The resulting representation is fed through a MLP comprised of two fully-connected layers. The first has a dimensionality of 512, the second has a dimensionality of $L = 128$ (generative modeling) or $L = 512$ (autoencoding and SVR).

All our NFs use coupling layers as their fundamental building blocks which translate and scale alternatingly odd/even dimensions where translation/scaling factors are computed as functions of even/odd dimensions. Scaling and translation factors are computed using two separate models applied to the masked input: linear layer (input dimension: d ; output dimension: D), 1-d Batchnorm, Swish activation function and a final linear layer (input dimension: D ; output dimension: d). In our conditional coupling layers the input is initially transformed by two separate models of the form: linear layer (input dimension: k ; output dimension: K), 1-d Batchnorm, Swish activation function and a final linear layer (input dimension: K ; output dimension: K). We then apply FiLM conditioning [38] where the condition is computed by a model of the form: linear layer (input dimension: L ; output dimension: K), 1-d Batchnorm, Swish activation function and a final linear layer (input dimension: K ; output dimension: K). Subsequently, scaling and translation are each fed through a ReLU activation function followed by a linear layer (input dimension: K ; output dimension: k).

Our learned *prior* is implemented as a normalizing flow consisting of 14 coupling layers. In these coupling layers we set $K = 128$ and $k = D$ (D : dimensionality of the latent space/bottleneck) since it needs to be of the same dimensionality as the latent space for reasons of invertibility (generative modeling: $d = 128$, autoencoding/SVR $d = 512$). When training on SVR we implement the prior model as a conditional NF. The condition is computed using an image encoder which is implemented as a ResNet18 [22].

Setting K and number of coupling in mixtures of NFs.

In order to ensure comparability between models based on a single NF and mixtures of NFs, we reduce the size of each NF in mixtures of NFs such it has slightly less parameters than a given reference model using a single NF. In particular, assume a single-flow-based model comprised of N coupling layers using a hidden dimensionality K . For a mixture of m NFs we compute the number of coupling layers \hat{N}

of each component in the mixture as $\hat{N} = \lceil \frac{N}{\sqrt{m}} \rceil$. Subsequently, we determine the hidden dimensionality \hat{K} of each component of the mixture by reducing K until the total number of parameters of the mixture model is smaller than the one of the single-flow-based model.

Optimization. We train all our models on Nvidia Titan RTX using ADAM [30] for 1450 (generation), 1050 (autoencoding) or 36 (SVR) epochs using a batch size of 36. We start each training with a learning rate of $2.56 \cdot 10^{-4}$ and divide it by four at certain epochs (generation: 800, 1200, 1400; autoencoding: 400, 800, 1000; SVR: 20, 30, 35).

Dataset. In order to provide a fair comparison with prior work, we conduct all the experiments using the ShapeNet dataset [6] provided by [33]. In our autoencoding experiments we use the ShapeNetCore.v2, which contains 55k point clouds subdivided into 55 classes. As for point cloud generation, we follow [54] and focus on three categories of the ShapeNet [6] dataset: *airplanes*, *cars*, and *chairs*. Finally, for single-view reconstruction we adopt the dataset from [9], which contains renders of shapes from the 13 classes of ShapeNetCore.v1. For each shape 24 images at a resolution of 137×137 are rendered from random viewpoints. The ground truth point clouds are obtained sampling from the original meshes. We randomly split per class in dataset into 70/10/20 proportion distributing to train/validation/test set for generation and autoencoding, for single-view reconstruction, we use the same train/test split from [9]. All experiments regarding generation and autoencoding are conducted on the normalized dataset provided by [33]. Similarly, for single-view reconstruction the models are trained on normalized data. However, we scale the data into a unit radius sphere during evaluation to ensure comparability with related work.

Visualization of F1-score We highlight the advantage of the F1-score as a convincing metric for perceptual quality by visualizing heatmaps of its components, precision and recall. fig. 8 provides two examples from which we can see that F1-score clearly focuses on high-frequency regions of the objects. We observe that for DPF the contributions to the F1-score primarily come from the high-frequency regions of an object, while in the case of mixtures of NFs the contributions are more evenly spread over the object.

Toy Example on the Advantages of Mixtures of Normalizing Flows

This section presents an analytic toy example demonstrating the advantages of using mixtures of NFs. There-

fore, consider the one-dimensional distributions in fig. 9:

$$p_Y(Y) = \begin{cases} 0.5 & \text{if } x < 1 \text{ and } x \geq -1 \\ 0 & \text{else} \end{cases} \quad (6)$$

$$p_X(X) = \begin{cases} 1 & \text{if } (x \geq 1 \text{ and } x < 2) \\ & \text{or } (x \geq -2 \text{ and } x < -1) \\ 0 & \text{else} \end{cases} \quad (7)$$

We wish to find an invertible transformation $f : Y \rightarrow X$ such that the change of variable formula

$$p_Y(Y) = p_X(f(Y)) \frac{df(Y)}{dY} \quad (8)$$

is satisfied. In this simple example we can directly write down the solution, namely

$$f(Y) = \begin{cases} 2 \cdot (Y - 1) & \text{if } x \leq 1 \\ 2 \cdot (Y + 1) & \text{if } x > 1 \end{cases} \quad (9)$$

Interestingly this function contains a discontinuity at 0. This discontinuity also implies an infinite bi-Lipschitz constant of the optimal solution as can be seen from the definition of the bi-Lipschitz constant K of a function g :

$$\frac{1}{K} |x_2 - x_1| \leq |g(x_2) - g(x_1)| \leq K |x_2 - x_1| \quad \forall x_1, x_2 \quad (10)$$

In the vicinity of the origin K has to approach infinity in order to fulfill above inequality. Attempting to learn such a discontinuous function using a neural network, which is only a universal function approximator for continuous functions, is difficult. However, we can bypass the discontinuity in this solution by utilizing two invertible maps, $f_1 = 4 \cdot (Y - 1.5)$ and $f_2 = 4 \cdot (Y + 1.5)$, and composing them as a mixture. Thus, we are introducing an additional continuous random variable w that identifies the invertible map responsible for a particular point $y \in Y$. This describes the underlying idea of applying mixtures of NFs to 3D data. By introducing additional latent variables we can empower our continuous model to avoid approximating discontinuous behaviour.

Further Results on Generative Modelling

Quantitative Results on Generative including Standard Deviation

We report quantitative metrics on generative modeling including their standard deviation in table 5.

Results on Generative Modelling with Reduced Model Size

We report quantitative (see table 6) and qualitative (see fig. 10) results on generative modeling using decoder models of reduced parameter counts for a single-flow-based

Category	Method	JSD \downarrow	MMD \downarrow		COV \uparrow		1-NNA \downarrow	
			CD	EMD	CD	EMD	CD	EMD
Airplane	l-GAN-CD [1]	2.76 \pm 0.16	5.69 \pm 0.04	5.16 \pm 0.02	39.5 \pm 0.8	17.1 \pm 0.6	72.9 \pm 0.8	92.1 \pm 0.6
	l-GAN-EMD [1]	1.77 \pm 0.13	6.05 \pm 0.04	4.15 \pm 0.02	39.7 \pm 1.4	40.4 \pm 1.2	75.7 \pm 0.6	73.0 \pm 1.2
	PointFlow [54]	1.42 \pm 0.12	6.05 \pm 0.05	4.32 \pm 0.01	44.7 \pm 1.2	48.4 \pm 1.0	70.9 \pm 1.0	68.4 \pm 1.0
	DPF [33]	1.14 \pm 0.08	<u>6.03</u> \pm 0.07	4.27 \pm 0.01	46.4 \pm 1.3	48.2 \pm 1.2	<u>70.3</u> \pm 1.2	<u>67.5</u> \pm 1.1
	Ours 4 Flows	1.03 \pm 0.09	6.06 \pm 0.06	<u>4.26</u> \pm 0.01	46.5 \pm 0.85	48.4 \pm 1.5	70.1 \pm 1.1	66.9 \pm 1.5
	Oracle	0.50 \pm 0.04	5.97 \pm 0.09	3.98 \pm 0.01	51.4 \pm 1.0	52.7 \pm 1.3	49.8 \pm 1.3	48.2 \pm 1.1
Chair	l-GAN-CD [1]	3.65 \pm 0.09	16.66 \pm 0.08	7.91 \pm 0.02	42.3 \pm 0.5	17.1 \pm 0.5	68.5 \pm 0.5	96.5 \pm 0.1
	l-GAN-EMD [1]	1.27 \pm 0.06	16.78 \pm 0.07	5.75 \pm 0.01	44.3 \pm 0.9	43.8 \pm 1.0	66.6 \pm 0.6	67.8 \pm 0.7
	PointFlow [54]	1.51 \pm 0.11	17.15 \pm 0.10	6.20 \pm 0.01	43.3 \pm 0.8	46.5 \pm 1.0	67.0 \pm 0.3	70.4 \pm 0.6
	DPF [33]	1.37 \pm 0.09	17.24 \pm 0.15	6.13 \pm 0.02	45.1 \pm 1.0	46.0 \pm 0.7	64.8 \pm 0.7	68.2 \pm 0.8
	Ours 4 Flows	1.45 \pm 0.09	17.30 \pm 0.12	<u>6.11</u> \pm 0.01	45.2 \pm 1.5	46.5 \pm 0.6	65.3 \pm 1.1	65.6 \pm 0.8
	Oracle	0.49 \pm 0.01	16.39 \pm 0.07	5.71 \pm 0.01	52.8 \pm 0.8	53.4 \pm 1.1	49.7 \pm 0.7	49.6 \pm 0.9
Car	l-GAN-CD [1]	2.65 \pm 0.07	8.83 \pm 0.06	5.36 \pm 0.01	41.3 \pm 0.8	15.9 \pm 1.3	62.6 \pm 0.6	92.7 \pm 0.4
	l-GAN-EMD [1]	1.31 \pm 0.10	9.00 \pm 0.08	4.40 \pm 0.01	38.3 \pm 1.2	32.9 \pm 0.7	65.2 \pm 0.4	63.2 \pm 1.0
	PointFlow [54]	0.59 \pm 0.02	9.53 \pm 0.06	4.71 \pm 0.01	42.3 \pm 1.0	35.8 \pm 1.3	70.1 \pm 0.9	74.2 \pm 0.6
	DPF [33]	0.57 \pm 0.04	9.67 \pm 0.08	<u>4.60</u> \pm 0.01	40.8 \pm 1.4	43.7 \pm 1.0	71.29 \pm 1.1	66.0 \pm 1.5
	Ours 4 Flows	0.55 \pm 0.03	9.50 \pm 0.1	<u>4.62</u> \pm 0.01	41.4 \pm 1.2	43.8 \pm 1.1	69.0 \pm 0.9	64.8 \pm 1.2
	Oracle	0.37 \pm 0.03	9.24 \pm 0.06	4.56 \pm 0.01	52.8 \pm 1.1	52.7 \pm 0.9	50.9 \pm 1.1	50.5 \pm 1.2

Table 5. Generative modeling. Comparison with related work. JSD and MMD-EMD are multiplied by 10^2 , MMD-CD is multiplied by 10^4

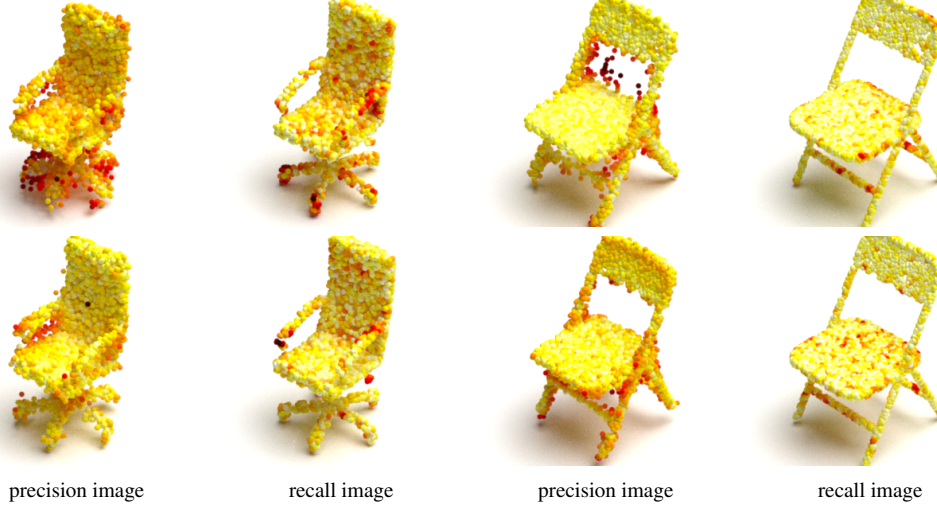


Figure 8. Visualization on precision and recall of the F1-score (TOP: DPF, BOTTOM: mixtures of 4 NFs). Points are considered to be more precise when the color is lighter in precision heatmap, meanwhile, points in the recall heatmap are lighter when the ground truth is well reconstructed by the model.

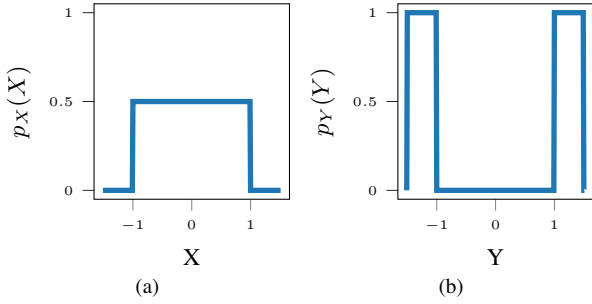


Figure 9. Probability distribution with uniform probability density in a given interval and zero probability density otherwise.

model and a mixture of 4 NFs. We reduce the parameter count by decreasing the number of coupling layers used by the normalizing flow (24, 12, 6). Note that the original model used in our main experiments contains 63 coupling layers. We observe that for 24 & 12 coupling layer the quantitative metrics on generative modeling remain largely unchanged while the quality of the generated samples (see fig. 10) and reconstruction performance (see main paper) clearly degrade. We only see a clear quantitative degradation in generative modeling performance when limiting the model to 6 coupling layers. We conclude that commonly used metrics for generative modeling struggle to represent perceptual quality of generated point clouds.

Interpolating Latent Representations

In fig. 11 and fig. 12, we show qualitative examples of interpolating between latent representations learned by our models trained on airplane, car and chair. We sample two point clouds (the left-most and the right-most in the fig. 11)

and map them on their latent representations using our encoder. Subsequently, we linearly interpolate between these latent representation and reconstruct the result using our decoder model which is based on a mixture of 4 NFs (see in fig. 11). Interestingly, our model also allows interpolating individual parts of one shape (see fig. 12).

Qualitative Results with Sparse Input

Here, we investigate whether mixtures of NFs can up-sample sparse point clouds. In fig. 13 we show qualitative examples. Following DPF [33], a sparse point cloud of 512 is upsampled to 32768 points. In line with previous results, mixtures of NFs yield better results in high-frequency regions.

Additional Qualitative Results on Generation

We show additional qualitative examples of generated point clouds using mixtures of NFs in fig. 14.

Additional Qualitative Results on Autoencoding

We show additional qualitative examples on autoencoding of point clouds using mixtures of NFs in fig. 15.

Additional Qualitative Results on SVR

We show additional qualitative examples on SVR of point clouds using mixtures of NFs in fig. 16.

Nr. coupling layers	Nr. of Flows	JSD ↓	MMD ↓		COV ↑		1-NNA ↓	
			CD	EMD	CD	EMD	CD	EMD
24	1	1.11	17.24	6.09	45.7	47.7	66.6	66.4
24	4	1.09	17.49	6.28	45.8	43.5	67.2	73.2
12	1	1.16	17.25	6.14	44.8	47.0	66.4	71.7
12	4	1.10	17.48	6.16	45.0	45.5	70.0	72.6
6	1	1.32	19.47	6.26	39.8	46.1	82.1	79.5
6	4	1.32	19.47	6.47	39.8	42.0	82.1	81.2

Table 6. Quantitative evaluation of generative modeling using a smaller decoder with (24, 12 & 6 coupling layers).

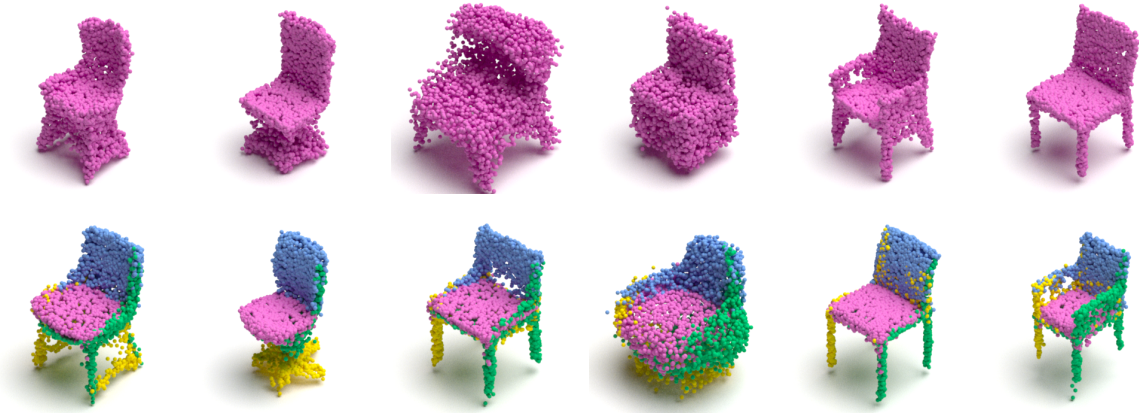


Figure 10. Qualitative results of generating point clouds using a decoder with 1 NF with 24 coupling layers (TOP) and 4 NFs with equivalent parameter count (BOTTOM).

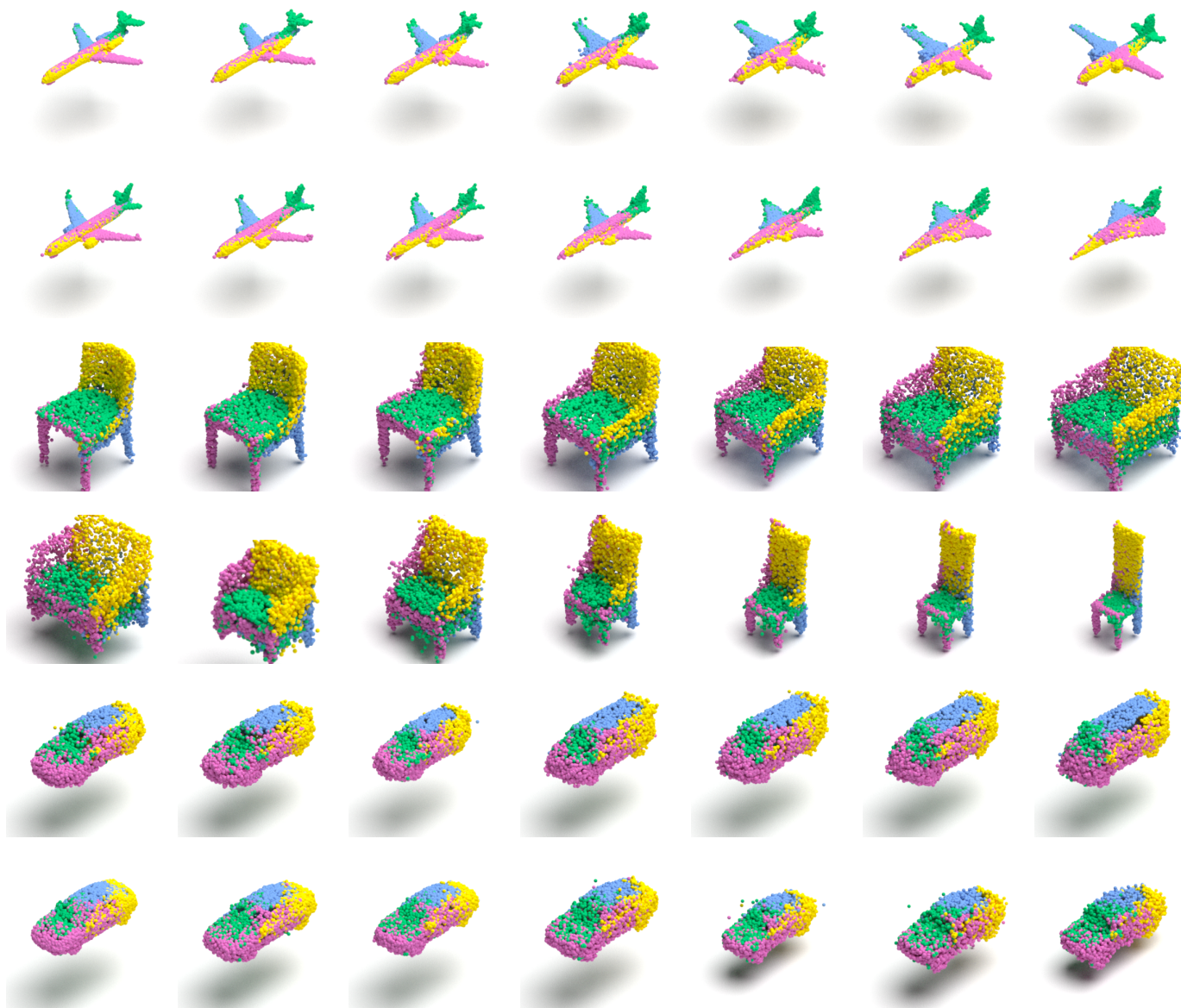


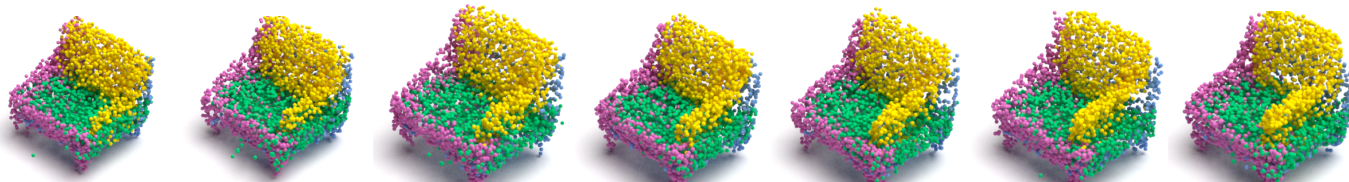
Figure 11. Qualitative examples of interpolation between two point clouds.



Interpolate the pink component



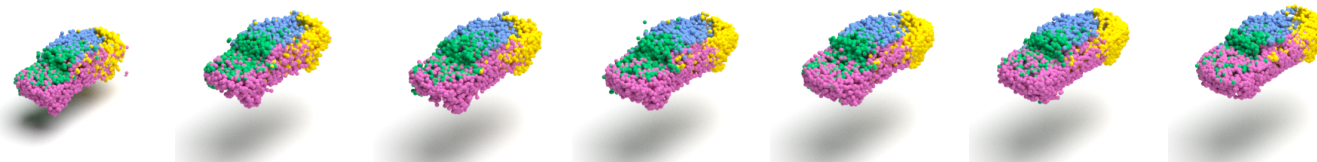
Interpolate the pink and blue components



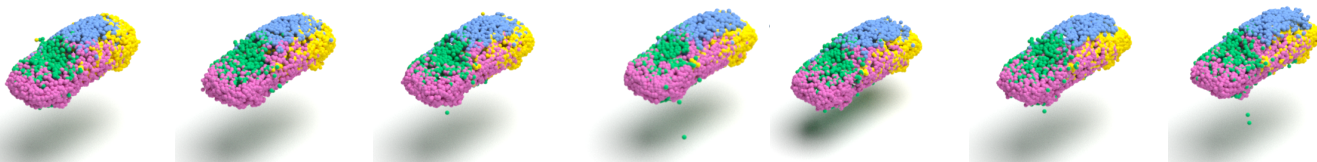
Interpolate the yellow component



Interpolate the yellow component



Interpolate the yellow and pink components



Interpolate the yellow and pink components

Figure 12. Qualitative examples of interpolating individual components of the mixture of NFs.

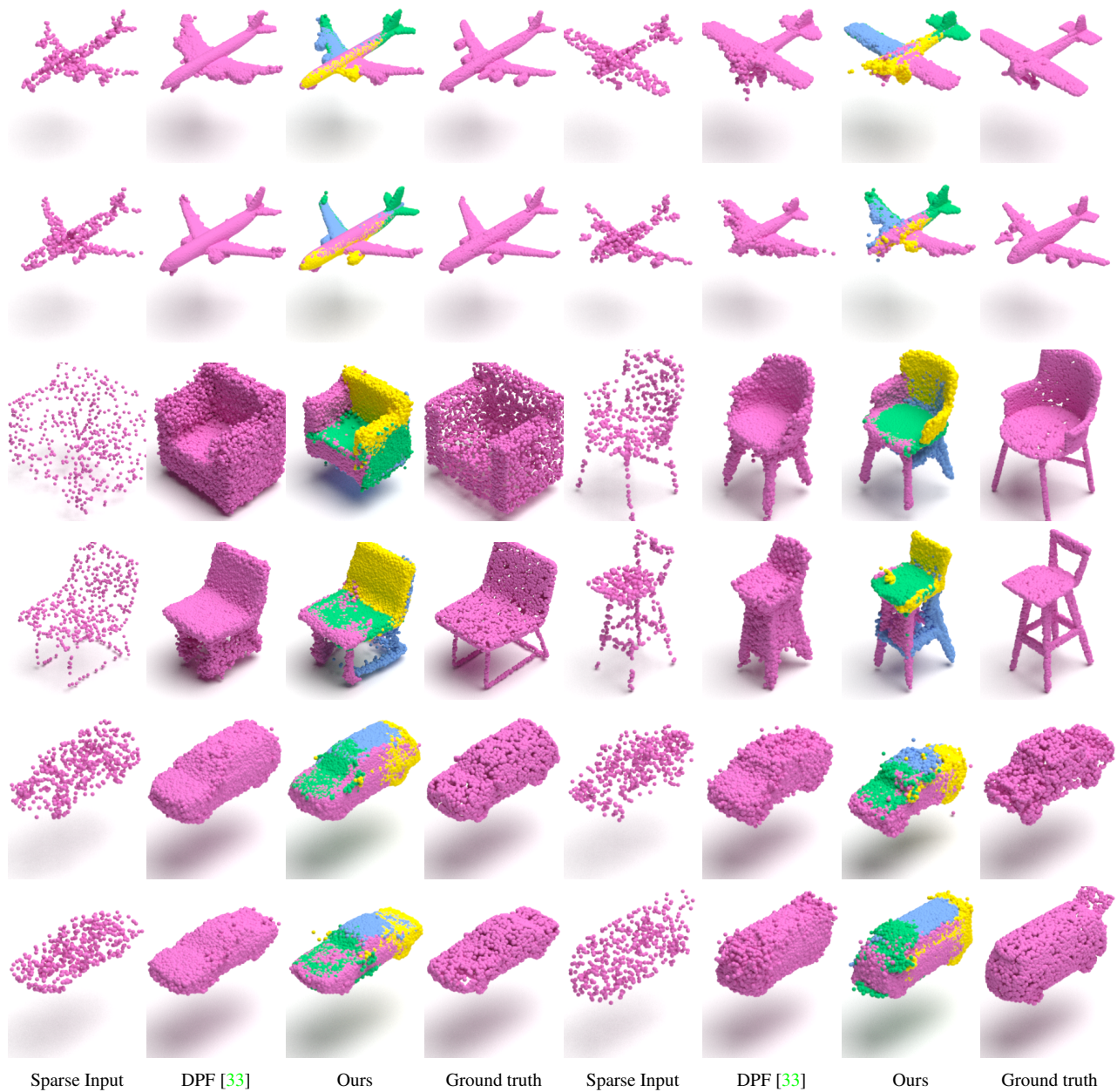


Figure 13. Qualitative examples of upsampling sparse point clouds.

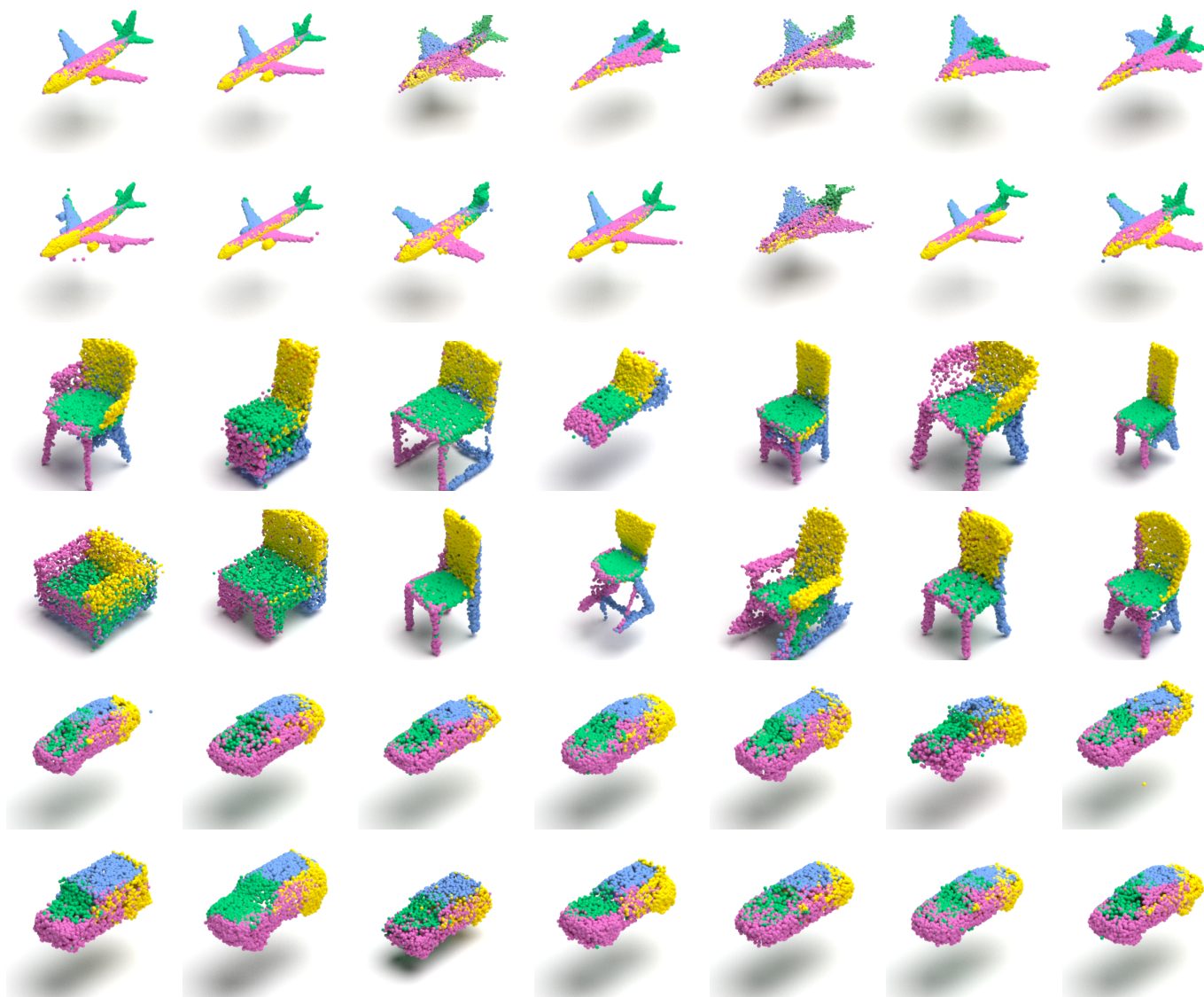
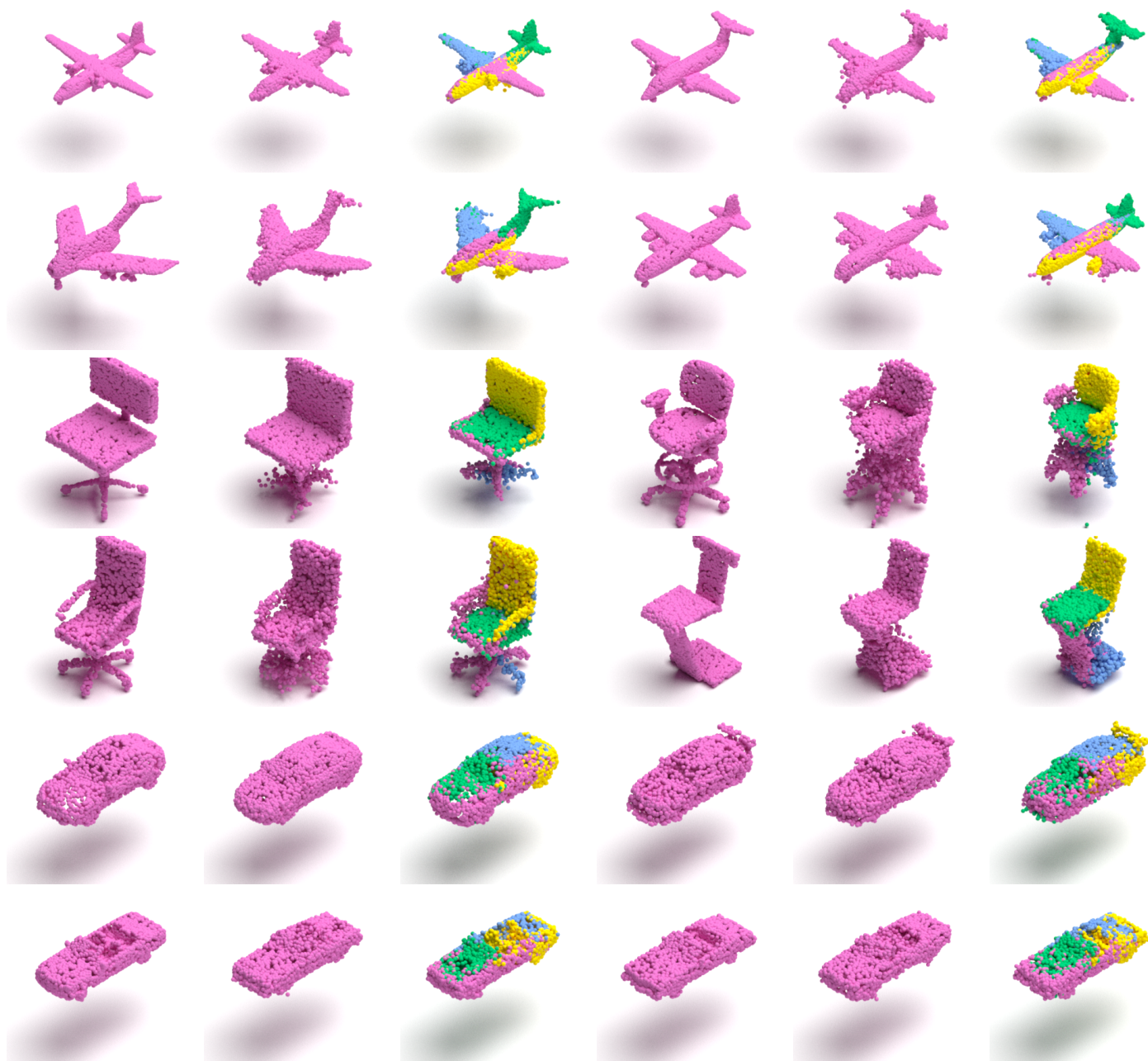


Figure 14. Additional qualitative examples of generated point clouds using mixtures of NFs.



Ground Truth

DPF [33]

Ours

Ground Truth

DPF [33]

Ours

Figure 15. Additional qualitative examples of autoencoding using mixtures of NFs.

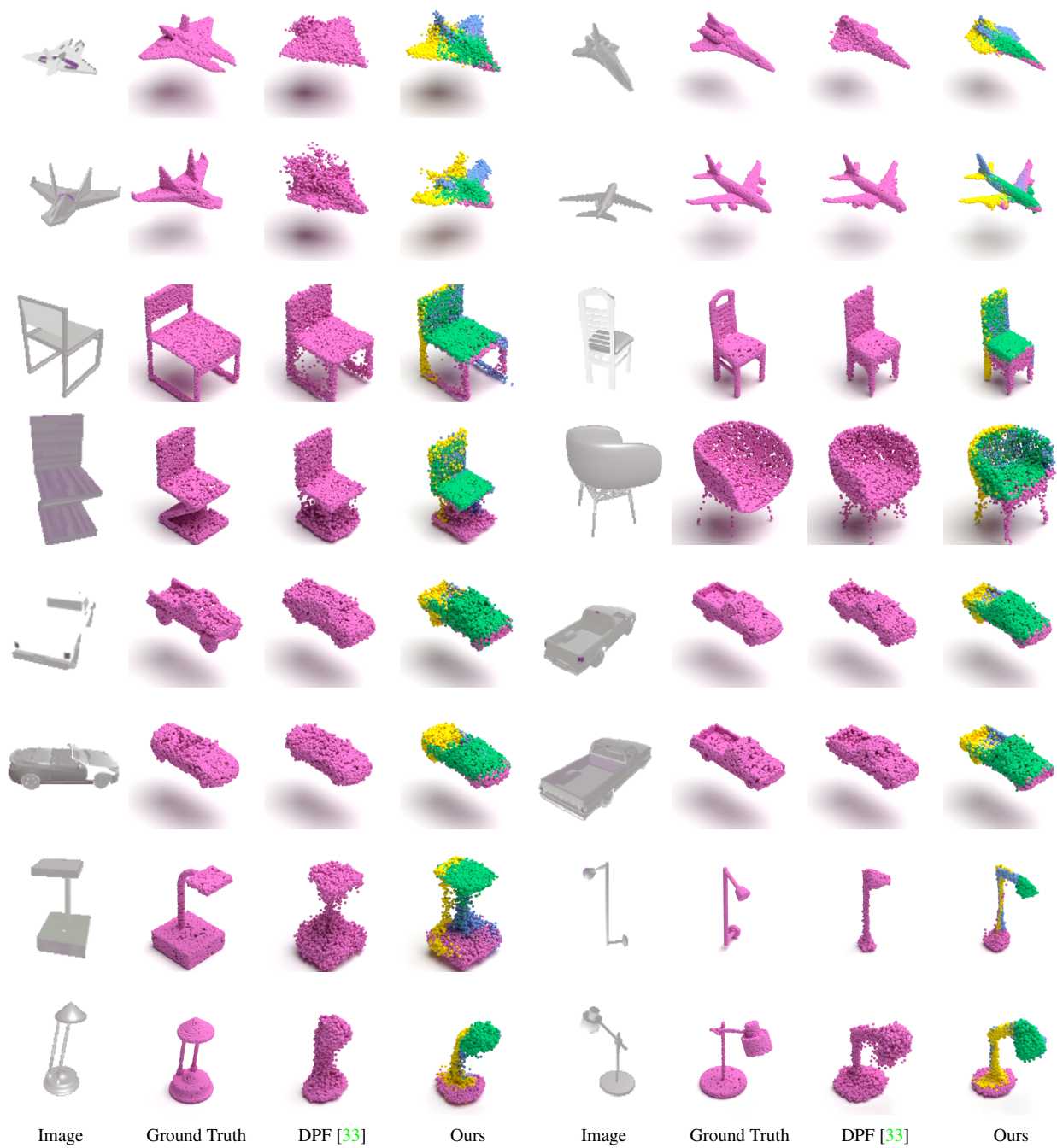


Figure 16. Additional qualitative examples of SVR using mixtures of NFs.